Dual effects of lone-pair electrons and rattling atoms in $CuBiS_2$ on its ultralow thermal conductivity

Zhenzhen Feng,[1,2] Tiantian Jia,[1,2] Jihua Zhang,[3] Yuanxu Wang,[4,*] and Yongsheng Zhang[1,2,†]

[1]*Key Laboratory of Materials Physics, Institute of Solid State Physics, Chinese Academy of Sciences, Hefei 230031, China*

[2]*Science Island Branch of the Graduate School, University of Science and Technology of China, Hefei 230026, China*

[3]*Guizhou Provincial Key Laboratory of Computational Nano-Material Science, Guizhou Education University, Guiyang 550018, China*

[4]*Institute for Computational Materials Science, School of Physics and Electronics, Henan University, Kaifeng 475004, China*

(Received 28 September 2017; published 18 December 2017)

Understanding the structural and physical origins of low thermal conductivity behavior is essential for improving and searching for high-efficiency thermoelectric materials. Natural minerals are cheap and usually have low thermal conductivities. The lattice thermal conductivities of two isostructural natural materials, chalcostibite $CuSbS_2$ and emplectite $CuBiS_2$, are substantially low in experimental measurements. In particular, the lattice thermal conductivity of $CuBiS_2$ is much lower than that of $CuSbS_2$. Using first-principles Debye-Callaway calculations, we found that the lattice thermal conductivities of $CuSbS_2$ and $CuBiS_2$ are 1.44 W/mK and 0.46 W/mK at 300 K, respectively, which are in good agreement with the experimental measurements. From the calculated vibrational properties, we demonstrate that the stereochemically active lone-pair electrons at the Sb sites are major contributors to the low thermal conductivity of $CuSbS_2$. However, for $CuBiS_2$, the dual effects of the lone-pair electrons at the Bi sites and the rattling of the Cu ions are the primary reasons for the ultralow thermal conductivity. Because of the ultralow thermal conductivity in $CuBiS_2$, our predicted highest ZT value in the material could reach 0.91 for n-type doping at 700 K and 0.77 for p-type doping at 780 K, which implies that $CuBiS_2$ can be utilized as a potential low-cost thermoelectric material for both n and p type. The present work emphasizes the importance of lone-pair electrons and rattling modes in impelling the phonon anharmonicity, providing a useful guide to seek and design new thermoelectric materials with ultralow thermal conductivity and high efficiency.

DOI: 10.1103/PhysRevB.96.235205

I. INTRODUCTION

Thermoelectric materials allow direct solid-state power conversion between thermal and electrical energy [1]. Thermoelectric properties are characterized by a dimensionless figure of merit $ZT = S^2\sigma T/\kappa$, where S is the Seebeck coefficient, σ is the electrical conductivity, T is the absolute temperature, and κ is the thermal conductivity, which is typically written as the sum of the electronic (κ_e) and lattice (κ_l) contributions: $\kappa = \kappa_e + \kappa_l$. A large figure of merit requires high S and σ but low κ. However, it is quite difficult to enhance the ZT value of a thermoelectric material since S and σ are strongly coupled via the carrier concentration.

There are two approaches generally used to improve thermoelectric performance. One is to enhance the electrical transport performance by modifying the band structures to obtain higher band degeneracy [2,3] or introduce the resonant level [4]. The other one is to decrease the thermal conductivity by controlling the various structural defects to scatter phonon effectively, such as alloying [5], grain boundaries [6], and nanostructures [7]. Recently, much attention has been focused on searching for thermoelectric materials with intrinsically low lattice thermal conductivity, originating from a complex crystal structure [8], large number of atoms [9], strong anharmonicity [10], or liquid-like (atomic rattling) behavior [11,12].

The widely investigated compounds, such as Ag-Bi-Se, Cu-Sb-S, or Cu-Sb-Se belong to a large family of natural minerals, which contains earth-abundant and environmentally friendly elements. Many compounds from the family exhibit intrinsically low lattice thermal conductivity and high thermoelectric performance. The low thermal conductivity results from the strong lattice anharmonicity or Umklapp phonon scatterings. For some I-V-VI_2 natural materials, such as $AgSbSe_2$ [13], $AgBiS_2$ [14], and $AgBiSe_2$ [15], the strong anharmonicity or low lattice thermal conductivity comes from the electrostatic repulsion between the stereochemically active s^2 lone pair of cations and the p-orbital of anions. The intrinsically low lattice thermal conductivity in Cu_3SbSe_3 [16] and $Cu_{12}Sb_4S_{13}$ [17] is due to the bond anharmonicity caused by the stereochemically active lone-pair electrons at the Sb sites. Qiu *et al.* [18] theoretically investigated the low lattice thermal conductivity behaviors of two Cu-Sb-Se compounds ($CuSbSe_2$ and Cu_3SbSe_3). The authors found that the lone-pair electrons at the Sb sites dominate the anharmonicity in $CuSbSe_2$. However, for Cu_3SbSe_3, they suggested that the liquid-like random diffusion of Cu atoms instead of lone-pair electrons has a great influence on the phonon anharmonicity. Since the two compounds have different crystal structures, it is difficult to identify the key role in the low lattice thermal conductivity. Therefore, understanding the determined chemical and physical factors for low lattice thermal conductivity in materials is the crucial issue for searching for and designing new materials with the low lattice thermal conductivity and high thermoelectric performance.

We thus focus on two isostructural natural mineral compounds ($CuMS_2$, M = Sb, Bi, called chalcostibite and emplectite) to understand the effects of lone-pair electrons and atomic rattling. The experimentally measured lattice thermal conductivities of the two compounds are intrinsically low at room temperature: 1.5 W/mK [19,20] and

*wangyx@henu.edu.cn

†yshzhang@theory.issp.ac.cn

0.5 W/mK [20,21] for $CuSbS_2$ and $CuBiS_2$, respectively. $CuMS_2$ (M = Sb, Bi) can be expressed as $Cu^+M^{3+}S_2^-$, which means that the outermost $3p$ electrons form covalent bonds with neighboring atoms, leaving the two s electrons as a lone pair like in $CuSbSe_2$. Although the two compounds are isostructural and both have the s^2 lone-pair electrons, the experimentally measured lattice thermal conductivity of $CuBiS_2$ is only a third of that of $CuSbS_2$. The origin of such different thermal conductivity behaviors has not been fully explored. Hence, it is imperative to understand the key factors for the ultralow thermal conductivity in $CuBiS_2$ and set up a detailed study of thermoelectric performance of the compound.

In this work, we investigate the vibrational properties of the two compounds using first-principles quasiharmonic phonon calculations. We find that the lone-pair electrons at the Sb sites in $CuSbS_2$ lead to a low lattice thermal conductivity. However, the ultralow κ_l of $CuBiS_2$ results from the lone-pair electrons at the Bi sites combined with the rattling modes of Cu atoms. Based on the theoretically calculated electrical transport properties (S and σ) and thermal conductivity, we find that the n-type $CuBiS_2$ possesses higher ZT value than the corresponding p-type one, which is mainly due to the larger band dispersion for the conduction band minimum or high σ. The maximum ZT of n-type $CuBiS_2$ is 0.91 at 700 K, suggesting that $CuBiS_2$ is a potential low-cost thermoelectric material. The present work helps guide further thermoelectric property optimization of $CuBiS_2$ and seek or design new sulfosalt systematics with stereochemically active lone-pair electrons combined with rattler atoms as efficient thermoelectric materials.

II. THEORETICAL METHODOLOGIES

A. Density functional theory calculations

The crystal structures of $CuSbS_2$ [19] and $CuBiS_2$ [22] were optimized utilizing the plane-wave projector augmented wave (PAW) method [23] using the Vienna *ab initio* simulation package (VASP) [24] based on density functional theory. The Perdew-Burke-Ernzerhof parametrization of the generalized-gradient approximation (PBE-GGA) was used for the exchange correlation potential. For total energy calculations, a plane-wave energy cutoff of 500 eV was employed throughout. For the sampling of the Brillouin zone, a $(9 \times 14 \times 3)$ Monkhorst-Pack [25] k-point mesh was used. The criterion of the energy convergence for electronic self-consistence is within 10^{-6} eV. The geometry relaxation was performed by relaxing both atomic positions and lattice constants. The crystal structure is considered to be in (local) minimum when the Hellmann-Feynman forces on each ion are less than 0.005 eV/Å.

The electronic structures of $CuSbS_2$ and $CuBiS_2$ were then calculated using the linearized augmented plane wave (LAPW) method [26,27], as implemented in the WIEN2k code [28]. The muffin-tin radii (R_{MT}) were set to 2.38, 2.5, 2.33, and 1.94 a.u. for Cu, Bi, Sb, and S, respectively. The cutoff parameter $R_{MT} \times K_{max} = 9$ (K_{max} is the magnitude of the largest k vector) was used, the self-consistent calculations were performed with the $(9 \times 14 \times 3)$ k mesh in the irreducible Brillouin zone, and the total energy was converged to within 0.0001 Ry. Since the local or semilocal exchange-correlation approximation underestimates band gaps due to the presence of artificial self-interaction and the absence of the derivative discontinuity in the exchange-correlation functional [29], accurate band gaps were calculated using the Tran-Blaha modified Becke-Johnson (TB-mBJ) functional [30]. The computed electronic structures with the TB-mBJ functional were further used to obtain electrical transport properties. The transport calculations were carried out using the semiclassical Boltzmann theory, as implemented in the BoltzTraP code [31], within the constant scattering time approximation, by taking 20 000 k points in the irreducible Brillouin zone.

The lattice dynamical properties of $CuSbS_2$ and $CuBiS_2$ were calculated using the frozen phonon method, as implemented in the Phonopy package [32]. A $(2 \times 3 \times 1)$ supercell (containing total 96 atoms) of $CuSbS_2$ and $CuBiS_2$ was constructed to ensure the convergence of the dynamic matrix. The Grüneisen parameters characterize the relationship between phonon frequency and volume change, which provides an estimation of the strength of anharmonicity in a compound. We calculated the Grüneisen parameters (γ) based on the quasiharmonic DFT phonon calculations, $\gamma_i = -\frac{V}{\omega_i}\frac{\partial \omega_i}{\partial V}$, in which the system volume is isotypically expanded by +2% from the DFT relaxed volume.

B. Lattice thermal conductivity

The Debye-Callaway model [33,34] was used to calculate the lattice thermal conductivity. According to the model, the lattice thermal conductivity (κ) is contributed by three acoustic modes: two transverse (κ_{TA} and $\kappa_{TA'}$) and one longitudinal (κ_{LA}) branch,

$$\kappa = \kappa_{TA} + \kappa_{TA'} + \kappa_{LA}. \tag{1}$$

For a perfect order crystalline without any defects or impurities, the dominant scattering mechanisms are the normal phonon scattering ($1/\tau_N$) and the Umklapp phonon scattering ($1/\tau_U$). The phonon relaxation time τ_c^{-1} is given by $\tau_c^{-1} = \tau_N^{-1} + \tau_U^{-1}$. κ_i (i corresponds to TA, TA′, or LA modes) can be written as [33,35]

$$\kappa_i = \frac{1}{3} C_i T^3 \left\{ \int_0^{\Theta_i/T} \frac{\tau_c^i(x) x^4 e^x}{(e^x-1)^2} dx + \frac{\left[\int_0^{\Theta_i/T} \frac{\tau_c^i(x) x^4 e^x}{\tau_N^i (e^x-1)^2} dx\right]^2}{\int_0^{\Theta_i/T} \frac{\tau_c^i(x) x^4 e^x}{\tau_N^i \tau_U^i (e^x-1)^2} dx} \right\}, \tag{2}$$

where Θ_i is the transverse or longitudinal acoustic Debye temperature, $x = \hbar\omega/\kappa_B T$, $C_i = \kappa_B^4/2\pi^2\hbar^3\upsilon_i$. Here, $\hbar$ is the Planck constant, κ_B is the Boltzmann constant, ω is the phonon frequency, and υ_i is the transverse or longitudinal acoustic phonon velocity.

The normal scattering process describes phonon-phonon scattering events in which momentum is conserved but phonons are redistributed. The phonon relaxation time for the normal process is [33,36]

$$\frac{1}{\tau_N^{TA/TA'}(x)} = \frac{\kappa_B^4\gamma_{TA/TA'}^2 V}{M\hbar^3\upsilon_{TA/TA'}^5}\frac{\kappa_B}{\hbar}xT^5, \tag{3}$$

$$\frac{1}{\tau_N^{LA}(x)} = \frac{\kappa_B^3\gamma_{LA}^2 V}{M\hbar^2\upsilon_{LA}^5}\left(\frac{\kappa_B}{\hbar}\right)^2 x^2T^5. \tag{4}$$

For the Umklapp scattering process, its relaxation time is given by

$$\frac{1}{\tau_U^i(x)} = \frac{\hbar\gamma^2}{M\upsilon_i^2\Theta_i}\left(\frac{\kappa_B}{\hbar}\right)^2 x^2T^3e^{-\Theta_i/3T}, \tag{5}$$

where V and M are the volume per atom and the average mass of an atom in the crystal, respectively.

C. Electrical transport properties

The electrical transport properties of a compound were investigated by solving the semiclassical Boltzmann transport equations. Note that except for the Seebeck coefficient S, the electrical conductivity σ, the power factor $S^2\sigma$, and the electrical thermal conductivity κ_e are all a function of the carrier relaxation time τ, which in principle is band structure and temperature dependent [37,38]. In practice, τ is often determined by fitting the experimental results. Alternatively, τ can also be systematically determined using first-principles calculations, by either explicitly considering the electron-phonon scattering mechanisms [37] or using the single parabolic band (SPB) model [39]. In the SPB model, the electron relaxation time is a function of energy (E) as

$$\tau = \tau_0\frac{2}{3}\left(r+\frac{2}{3}\right)\frac{F_{r+1/2}(E^*)}{F_{1/2}(E^*)} = \tau_0E^r, \tag{6}$$

where τ_0 is energy independent but it depends on effective mass and temperature, and r is the scattering parameter. The Fermi integral $F_x(E^*)$ is represented as

$$F_x(E^*) = \int_0^\infty \frac{E^{*x}}{1+exp(E^*-E_F^*)}dE, \tag{7}$$

where E^* is the reduced energy ($E^* = E/\kappa_B T$). At moderate temperature, electrons are scattered by acoustic modes and $r = -1/2$. Then the carrier relaxation time is given by

$$\tau = \frac{2^{1/2}\pi\hbar^4\rho\upsilon_l^2}{3E_d^2(m^*\kappa_B T)^{3/2}}\frac{F_0(E^*)}{F_{1/2}(E^*)}, \tag{8}$$

where υ_l is the longitudinal sound velocity, E_d is the deformation potential constant, m^* is the single valley DOS effective mass, E_F^* is the reduced chemical potential ($E_F^* = E_F/\kappa_B T$), and ρ is the mass density.

Then the directional carrier mobility μ can be determined by $\mu = \tau e/m_i^*$, where m_i^* is the effective mass along the direction i. Once the mobility μ is known, the electrical conductivity can be obtained from $\sigma = ne\mu$, where n is the carrier density. The electronic thermal conductivity $\kappa_e^i = L\sigma_i T$, where the Lorenz number L is determined from the Boltzmann transport equation. The effective masses $m_{k,l}^* = \hbar^2/[\partial^2E/\partial k_k\partial k_l]$ for electrons and holes along the three directions were calculated near the band extrema. The longitudinal sound velocities were obtained using the phonon dispersions near the Γ point. The deformation potential constant is defined as $E_d^i = \Delta V_i/(\Delta l/l_0)$, where ΔV_i is the energy change of the ith band with the lattice dilation $\Delta l/l_0$ along the direction of d. In general, we take the energy change at the valence band maximum (VBM) and the conduction band minimum (CBM) for holes and electrons, respectively, with a series of lattice constants $(0.99a_0, 0.995a_0, a_0, 1.005a_0, 1.01a_0)$. The difficulty in theoretical calculation of the absolute deformation potential is that the reference of an energy level in an infinite periodic crystal is ill defined. To overcome this problem, we followed the approach proposed by Wei and Zunger [40], which assumes that the energy level of the deep core state is not sensitive to the slight lattice deformation. Therefore, it could be used as the reference to obtain the absolute band edge shifts.

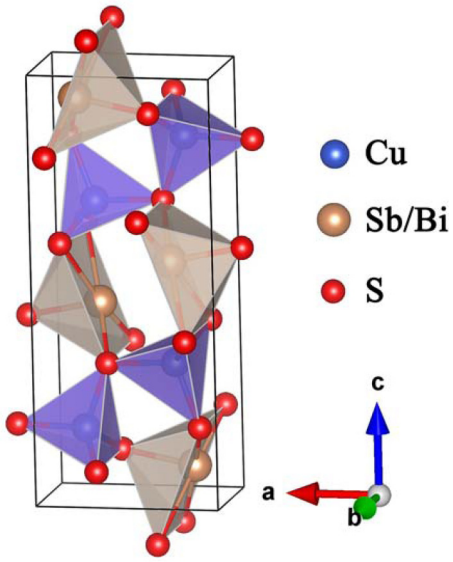

FIG. 1. Crystal structure of $CuMS_2$ (M = Sb, Bi), with Cu, M, and S atoms shown as blue, brown, and red spheres, respectively. The gray square pyramid and purple tetrahedra indicate the MS_5 and CuS_4 geometries, respectively.

III. CRYSTAL STRUCTURE AND BONDING PROPERTIES

Figure 1 shows the optimized crystal structures of $CuMS_2$ (M = Sb, Bi). $CuMS_2$ forms a stable orthorhombic structure (space group $Pnma$), with the lattice parameters $a = 6.134$ Å, $b = 3.830$ Å, and $c = 14.475$ Å for $CuSbS_2$, and $a = 6.293$ Å, $b = 3.953$ Å, and $c = 14.457$ Å for $CuBiS_2$, which are in agreement with the experimental values [19,22]. The two structures are composed of square pyramidal MS_5 and nearly regular CuS_4 tetrahedra as shown in Fig. 1. The Sb-S bond lengths (3.12, 3.12, 2.48, 2.61, 2.61 Å) in the SbS_5 square pyramid in $CuSbS_2$ are shorter than the corresponding Bi-S

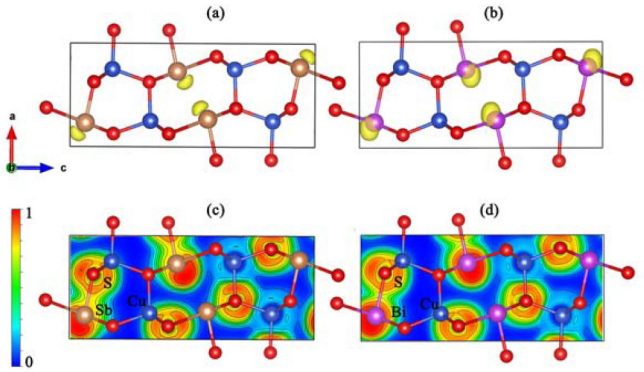

FIG. 2. Electronic localization function (ELF) of (a) $CuSbS_2$ and (b) $CuBiS_2$. The isosurface level is 0.93. The ELF of (c) $CuSbS_2$ and (d) $CuBiS_2$ are projected onto the (101) plane.

bond lengths (3.13, 3.13, 2.61, 2.70, 2.70 Å) in $CuBiS_2$, which implies that the Bi-S bond could be relatively weak.

To understand the bonding character in $CuMS_2$ (M = Sb, Bi), we calculated the electron localization function (ELF) [41]. The ELF can be expressed as $\mathrm{ELF}(\mathbf{r}) = \{1 + [K(\mathbf{r})/K_h(\rho(\mathbf{r}))]^2\}^{-1}$, where K is the curvature of the electron pair density for electrons of identical spin, $\rho(\mathbf{r})$ is the density at $\mathbf{r}$, and $K_h[\rho(\mathbf{r})]$ is the value of K in a homogeneous electron gas with density ρ. The ELF has often been used to characterize the degree of electron localization to quantitatively identify the character of chemical bonds between atoms. The ELF value lies by definition between zero and 1. ELF = 0 corresponds to no localization (regions without any electron), ELF = 0.5 reflects the behavior of a homogeneous electron distribution (as found in regions where the bonding has a metallic character), and ELF = 1 indicates full localization (as found in regions of covalent bonds, core shells, and lone pairs).

Figures 2(a) and 2(b) show the calculated 3D ELF (isosurface level of 0.93) of $CuSbS_2$ and $CuBiS_2$, respectively. The "mushroom" ELF shape around Sb/Bi is a clear indicator of the existence of lone-pair electrons. In addition, the electron sharing can be better visualized using the 2D ELF map in Figs. 2(c) and 2(d): the ELF of Sb/Bi lone pairs is in the shape of bean. Moreover, the lone-pair electrons are mainly located along the a and c axes. The electronic repulsion between the lone-pair electrons and Sb-S/Bi-S bonding electrons could lead to strong anharmonicity along the two axes in $CuSbS_2$ and $CuBiS_2$. According to the valence shell electron pair repulsion (VSEPR) theory [42], the lone-pair electrons like to take up one bonding site. Thus, in $CuMS_2$, the coordination environment of M is five bonds to the S atoms arranged in a square pyramid and one vacant site occupied by the lone-pair electrons (Fig. 1). The MS_5 (M = Sb, Bi) square pyramids undergo considerable local distortions (the Sb-S bond lengths: 3.12, 3.12, 2.48, 2.61, 2.61 Å, and the Bi-S bond lengths: 3.13, 3.13, 2.61, 2.70, 2.70 Å). The large asymmetric distortion of the MS_5 square pyramids could indicate the possibility of strong anharmonicity, which can significantly enhance heat carrying phonon scattering and reduce lattice thermal conductivity. Furthermore, the interstitial electrons between Cu and S and between Bi/Sb and S are localized close to the S atoms, as expected from the larger Pauling electronegativity value [43] of S (2.5) compared with Cu (1.9) and Sb (2.05)/Bi (2.02). The ELF value of the area between Sb and S is approximately 0.75, larger than that between Bi and S (0.68), which suggests a weak bonding between Bi and S atoms. The weak bonding of Bi-S is consistent with the fact that the bond length of Bi-S in $CuBiS_2$ is longer than the bond length of Sb-S in $CuSbS_2$. The weak bonding of Bi-S in $CuBiS_2$ may lead to a lower lattice thermal conductivity than in $CuSbS_2$.

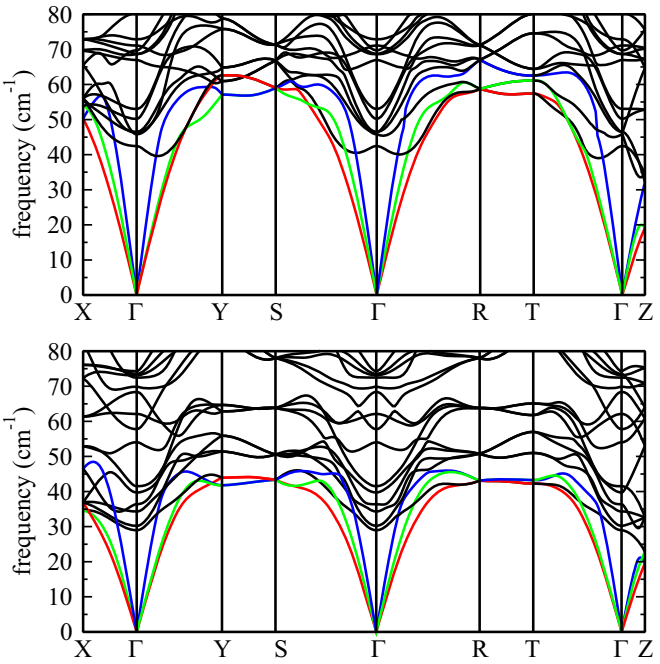

FIG. 3. Phonon dispersions of (a) $CuSbS_2$ and (b) $CuBiS_2$. The red, green, and blue lines highlight two transverse (TA, TA′) and one longitudinal (LA) acoustic mode, respectively. The high-symmetry k points X, Γ, Y, S, R, T, and Z represent (0.5, 0, 0), (0, 0, 0), (0, 0.5, 0), (0.5, 0.5, 0), (0.5, 0.5, 0.5), (0, 0.5, 0.5), and (0, 0, 0.5), respectively.

IV. PHONON PROPERTIES

A. Phonon dispersions and atomic displacement parameters

Acoustic phonon dispersions strongly influence the thermal transport properties. Figures 3(a) and 3(b) show the phonon dispersions of $CuSbS_2$ and $CuBiS_2$ along high-symmetry directions in their corresponding Brillouin zones. The real frequencies of all modes indicate that the two crystals are thermodynamically stable. Since the acoustic modes are largely responsible for heat transport, we highlight these modes with different colors in the plots. For the two compounds, the acoustic branches are overlapping with the optical branches near the BZ boundaries, leading to strong acoustic-optical interactions and highly nonlinear dispersion curves. The acoustic modes along the a (Γ-X) and c (Γ-Z) axes are softer than those along the b (Γ-Y) axis. These soft modes are mainly due to the stereochemically active lone-pair electrons at the Sb and Bi atoms, which are mainly along the a and c directions. Moreover, the acoustic phonon modes of $CuBiS_2$ are softer than those of $CuSbS_2$, which indicates $CuBiS_2$ having the low Debye temperature and low phonon velocity. Using the phonon

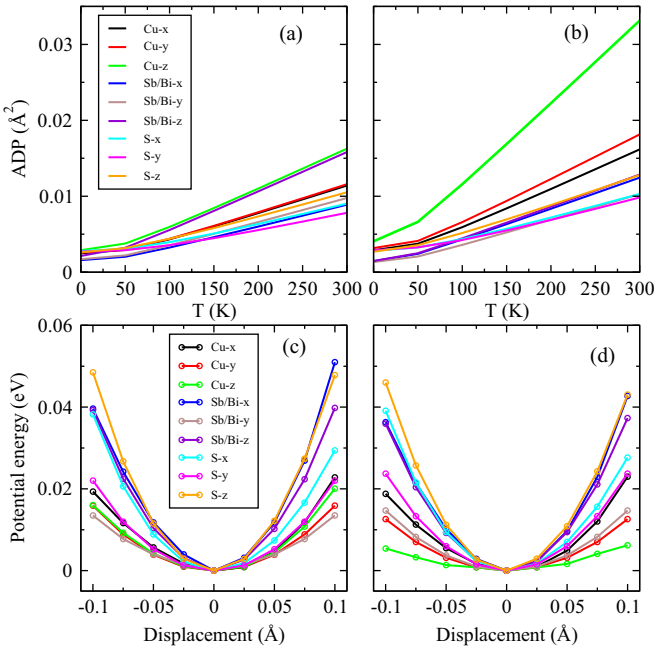

FIG. 4. Calculated atomic displacement parameters (ADPs) for (a) $CuSbS_2$ and (b) $CuBiS_2$. The calculated potential energy curves for all the atoms as a function of displacement around the equilibrium positions along the x, y, and z directions for (c) $CuSbS_2$ and (d) $CuBiS_2$.

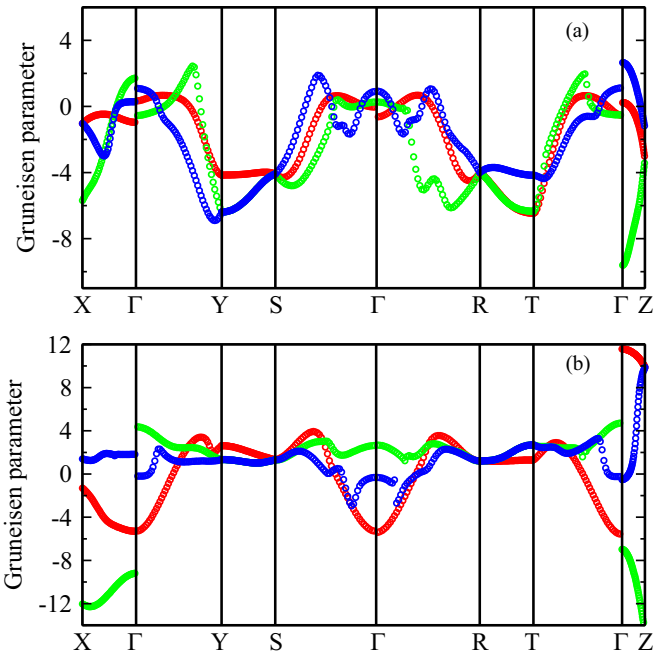

FIG. 5. Calculated Grüneisen dispersions for (a) $CuSbS_2$ and (b) $CuBiS_2$. The TA, TA′, and LA modes are shown as red, green, and blue lines, respectively.

dispersions (Fig. 3), the calculated two transverse (TA, TA′) and one longitudinal (LA) Debye temperatures are 70.1, 81.8, and 87.9 K for $CuSbS_2$, and are 63.4, 62.8, and 78.1 K for $CuBiS_2$. The phonon velocity can be calculated using the slope of the phonon dispersion around the Γ point. For $CuSbS_2$, the transverse phonon velocities are 2244 and 2877 m/s, and the longitudinal mode propagates at a higher speed of 4316 m/s. The corresponding phonon velocities for $CuBiS_2$ are slower: 1690, 2064, and 3457 m/s, respectively (Table I). The low Debye temperature and slow speed of sound in $CuBiS_2$ may lead to a low lattice thermal conductivity.

The atomic displacement parameter (ADP) assesses the mean-squared displacement amplitudes of an atom around its equilibrium position in a crystal and reflects the strength of the chemical bond. Usually, a relatively large ADP value implies that the corresponding atom vibrates more frequently around its equilibrium position than other atoms, indicating weak restoring forces on the vibrating atoms or the weak bonding [18,44,45]. As shown in Figs. 4(a) and 4(b), the ADPs of atoms in $CuSbS_2$ are small (<0.02 Å^2), which means that none of the atoms in $CuSbS_2$ have relatively weak bonds [44,45]. The ADPs of Cu are highly anisotropic with the maximum vibration along the z axis. The thermally induced ADPs of Cu atoms along the z direction are larger than those of other atoms. In particular, the ADP of Cu-z in $CuBiS_2$ has the significantly largest value. The large anisotropic atomic displacement parameters suggest that Cu atoms behave as rattlers in $CuBiS_2$. Additionally, from the potential energy surfaces, shifting atoms away from their equilibrium positions along the x, y, and z directions, as seen in Figs. 4(c) and 4(d), the Cu and other atoms in $CuSbS_2$ sit in deep potential wells. However, we found that the potential energy surface of the off-centered Cu atom in $CuBiS_2$ along the z direction is very flat. The large ADPs of Cu atoms in $CuBiS_2$ indicate that they are loosely bound in the lattice. Thus, in addition to the lone-pair electrons at the Bi sites, the Cu ratters could strengthen crystal anharmonicity, further scattering phonons and resulting in even lower lattice thermal conductivity.

B. Grüneisen parameters

To explore the thermal conductivity within the Debye-Callaway model, the important Grüneisen parameter is required to be calculated. It is known that the Grüneisen parameter provides valuable insight into the lattice anharmonicity and is thus beneficial to analyze the physical nature of lattice thermal conductivity behavior [16,46]. To quantitatively evaluate the anharmonicity, we plot the dispersion of the Grüneisen parameters of acoustic modes of $CuMS_2$ (M = Sb, Bi), as illustrated in Fig. 5. The most noteworthy feature of the dispersions in Fig. 5(b) is the unusually high values of the Grüneisen parameters in $CuSbS_2$ and $CuBiS_2$ along the Γ-X and Γ-Z directions, especially for $CuBiS_2$. As we mentioned before, the lone-pair electrons at the Sb/Bi sites are mainly along the two directions. Thus, the lone-pair electrons play an important role in the large Grüneisen parameters along the x and z directions in the two compounds. Since the two compounds are isostructural, if the lone-pair electrons were the only dominant role in the anharmonicity, the two compounds would have similar Grüneisen parameters. However, we found that the Grüneisen parameters along the x and z directions in $CuBiS_2$ are significantly larger than those in $CuSbS_2$. The larger Grüneisen parameters in $CuBiS_2$ result from the stronger atomic rattling: the rattling of all atoms along x and z directions in $CuBiS_2$ are larger than those in $CuSbS_2$ (Fig. 4). The large

TABLE I. Summary of average transverse (TA/TA′) and longitudinal (LA) Grüneisen parameters ($\overline{\gamma}_{TA/TA'/LA}$), Debye temperatures ($\Theta_{TA/TA'/LA}$), and phonon velocities ($\upsilon_{TA/TA'/LA}$) for $CuSbS_2$ and $CuBiS_2$. The Debye temperature is calculated using $\Theta = \omega_D/\kappa_B$ (ω_D is the largest acoustic frequency in each direction); the phonon velocity is the slope of the acoustic phonon dispersion around the Γ point.

System	$\overline{\gamma}_{TA}$	$\overline{\gamma}_{TA'}$	$\overline{\gamma}_{LA}$	Θ_{TA} (K)	$\Theta_{TA'}$ (K)	Θ_{LA} (K)	υ_{TA} (m/s)	$\upsilon_{TA'}$ (m/s)	υ_{LA} (m/s)
$CuSbS_2$	1.29	2.51	1.63	70.1	81.8	87.9	2244	2877	4316
$CuBiS_2$	3.85	4.48	2.17	63.4	62.8	78.1	1690	2064	3457

values of the Grüneisen parameters in $CuBiS_2$ imply that its acoustic branches are strongly anharmonic.

We further calculated the average Grüneisen parameters ($\overline{\gamma}$) of each acoustic dispersion ($\overline{\gamma} = \sqrt{\langle\gamma_i^2\rangle}$), as listed in Table I. The average acoustic Grüneisen parameters are $\overline{\gamma}_{TA} = 1.29$, $\overline{\gamma}_{TA'} = 2.51$, and $\overline{\gamma}_{LA} = 1.63$ in $CuSbS_2$. The corresponding values for $CuBiS_2$ are 3.85, 4.48, and 2.17. The further averages of the acoustic γ of the two compounds are around 1.81 and 3.5, respectively. These values are comparable to the average Grüneisen parameters of low lattice thermal conductivity compounds, such as $AgSbTe_2$ (2.05) [47] and β-Zn_4Sb_3 (1.57) [47]. Thus, the large Grüneisen parameters in $CuMS_2$ (M = Sb, Bi) indicate strongly anharmonic vibrational properties and low lattice thermal conductivity. In addition, the acoustic $\overline{\gamma}$ in $CuBiS_2$ is much larger than that in $CuSbS_2$. This indicates that $CuBiS_2$ has even stronger anharmonicity and lower thermal conductivity than $CuSbS_2$.

C. Lattice thermal conductivity

The Debye-Callaway approach calculates the temperature-dependent lattice thermal conductivity of $CuSbS_2$ (M= Sb, Bi) [Fig. 6(a)]. The theoretically evaluated κ_l for $CuSbS_2$ and $CuBiS_2$ are 1.44 W/mK and 0.46 W/mK at room temperature, respectively. These values are in good agreement with those from experimental measurements [19–21] (1.5 W/mK and 0.5 W/mK for $CuSbS_2$ and $CuBiS_2$, respectively). For $CuSbS_2$, the lone-pair electrons at the Sb sites dominate the anharmonicity and lead to a low thermal conductivity. However, except for the lone-pair electrons at the Bi sites, the Cu ions rattling can further raise the Grüneisen parameters. The dual effects of lone-pair electrons and rattling atoms are the major reason for the ultralow thermal conductivity of $CuBiS_2$.

For $CuBiS_2$ with the ultralow lattice thermal conductivity, we further explored the lattice thermal conductivity behavior along three different directions (a, b, and c). As shown in Fig. 6(b), the lattice thermal conductivities of $CuBiS_2$ are anisotropic: the calculated room temperature κ_l of $CuBiS_2$ along the a, b, and c axes is 0.64, 0.88, and 0.25 W/mK, respectively. The lower κ_l along x and z directions is attributed to larger Grüneisen parameters along the two directions (Fig. 5).

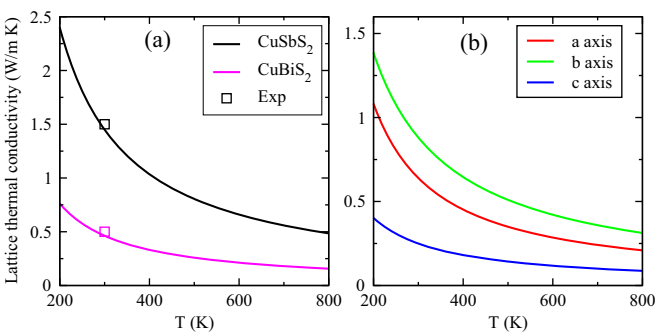

FIG. 6. (a) Calculated lattice thermal conductivity (κ_l) of $CuMS_2$ (M = Sb, Bi). (b) Calculated κ_l along the a, b, and c axes of $CuBiS_2$.

V. ELECTRICAL PROPERTIES

Owing to the same outermost valence electrons (three p and two s electrons) of Sb and Bi, the band structures (Fig. 7 and Fig. S1 in the Supplemental Material [48]) and the effective masses (Table II and Table S1 in the Supplemental Material [48]) of the $CuSbS_2$ and $CuBiS_2$ compounds are similar, indicating the similar electrical transport properties. Since the lattice thermal conductivity of $CuBiS_2$ is ultralow, it is worthwhile to especially study its electrical transport properties to determine whether it can be used as a thermoelectric material. The electronic structure is crucial for analyzing the electrical transport properties. Figure 7 shows the calculated electronic band structures of $CuBiS_2$ using the mBJ correction along the high-symmetry directions. $CuBiS_2$ is a semiconductor with 0.73 eV indirect band gap in the calculation, which is in reasonable agreement with experimentally measured 1.1 eV [49]. The CBM is at (0.29, 0, 0) along the Γ-X direction and the VBM is at the Γ point. At room temperature, the large band gap is sufficient to prevent bipolar conduction for the doped materials. Thus, the correction of the band gap to the experimental value would not change our conclusions significantly. The calculated band effective masses (m^*) are

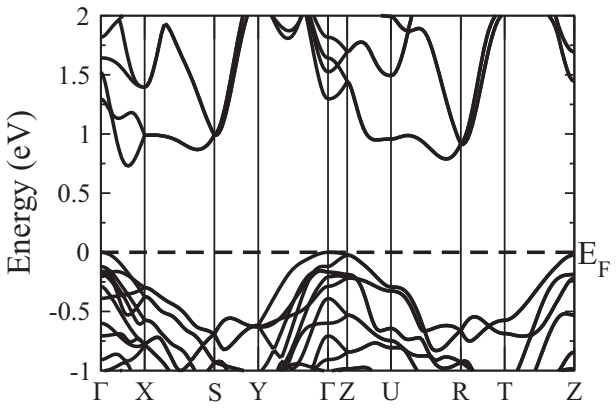

FIG. 7. Electronic band structures of $CuBiS_2$. The high-symmetry k points Γ, X, S, Y, Z, U, R, and T represent (0, 0, 0), (0.5, 0, 0), (0.5, 0.5, 0), (0, 0.5, 0), (0, 0, 0.5), (0.5, 0, 0.5), (0.5, 0.5, 0.5), and (0, 0.5, 0.5), respectively.

TABLE II. The calculated effective masses (m^*), deformation potential constants (E_d), and longitudinal sound velocities (υ_l) along the x, y, and z directions used for the SPB model to evaluate the electrical transport properties of $CuBiS_2$.

		m^* (m_0)			E_d (eV)			υ_l (m/s)		
System	Carrier	x	y	z	x	y	z	x	y	z
$CuBiS_2$	VBM	2.63	2.86	3.10	4.01	3.76	5.76	3964	3637	2702
	CBM	0.26	0.65	0.50	3.01	2.73	9.37			

given in Table II. It is well known that the light mass band is beneficial to large electrical conductivity, while the heavy mass band is favorable for a good Seebeck coefficient S. The VBM of $CuBiS_2$ has larger band degeneracy and band effective mass than those at the CBM, which is conducive to obtaining large Seebeck coefficients for p-type $CuBiS_2$, as can be identified from Fig. 8. However, the band effective masses of the VBM in all directions in $CuBiS_2$ are significantly higher than those of the CBM (Table II), which suggests low hole mobility but high electron mobility in $CuBiS_2$. High electron mobility is helpful to achieve a higher electrical conductivity for n-type $CuBiS_2$ than the hole conductivity for the p-type one.

The calculated electrical conductivities and Seebeck coefficients as a function of carrier concentration at 300, 400, 500, 600, 700, and 780 K ($CuBiS_2$ melts at approximately 780 K [50]) are illustrated in Fig. 8. The average electrical conductivities are calculated by $\overline{\sigma} = (\sigma_a + \sigma_b + \sigma_c)/3$. We found that the electrical conductivity of n-type $CuBiS_2$ is larger than the hole conductivity of the p-type one [Figs. 8(a) and 8(d)], due to the large conduction band dispersion or small electron effective mass (Table II) near the Fermi level. For the Seebeck coefficient (S), it decreases with increasing carrier concentration or with decreasing temperature. The S of p-type $CuBiS_2$ is larger than that of the n-type one [Figs. 8(b) and 8(e)]. This behavior is due to the heavy hole effective masses (Table II) and large band degeneracy (Fig. 7), which can be seen directly from the Mott formula

$$S = \frac{\pi^2 \kappa_B^2 T}{3e}\left\{\frac{d\{\ln[\sigma(E)]\}}{dE}\right\}_{E=E_F} = \frac{\pi^2 \kappa_B^2 T}{3e}\left\{\frac{1}{n}\frac{dn(E)}{dE} + \frac{1}{\mu}\frac{d\mu(E)}{dE}\right\}_{E=E_F}, \quad (9)$$

where $n(E)$ and $\mu(E)$ represent the carrier density and mobility, respectively. Increasing the density of states near the Fermi level or increasing band degeneracy could achieve a large Seebeck coefficient for p-type $CuBiS_2$.

With all the transport coefficients available, we can evaluate the figure of merit (ZT) of $CuBiS_2$. To calculate the averaged $\overline{ZT}$, the power factor is averaged over the three directions by $\overline{PF} = (S_a^2\sigma_a + S_b^2\sigma_b + S_c^2\sigma_c)/3$. Figures 8(c) and 8(f) show the calculated ZT values of $CuBiS_2$ at different temperatures. Because doping generally benefits the electrical conductivity while it deteriorates the Seebeck coefficient, the ZT value will first increase and then decrease with the carrier concentration, consequently leading to an optimal value. The calculated ZT of n-type $CuBiS_2$ is larger than that of the p-type one at the optimum carrier concentration due to the larger electrical conductivity of the n-type one. As seen in Figs. 8(c) and 8(f), the maximum ZT for p-type and n-type $CuBiS_2$ is 0.77 at 780 K (2.16×10^{20} holes/cm^3) and 0.91 at 700 K (1.04×10^{19} electrons/cm^3), respectively. The ZT values can be compared with a natural mineral tetrahedra-based compound $Cu_{12}Sb_4S_{13}$ (a promising thermoelectric material), and the Mn-doped $Cu_{12}Sb_4S_{13}$ has the highest ZT value of approximately 1.13 at 575 K [51]. For the $CuSbS_2$ compound, its electrical transport behaviors (S and σ) are similar to those in $CuBiS_2$ (Fig. 8 and Fig. S2 in the Supplemental Material [48]). Due to the higher thermal conductivity of $CuSbS_2$, it has a slightly worse thermoelectric performance than $CuBiS_2$: the maximum ZT for p-type and n-type $CuSbS_2$ are 0.67 (3.7×10^{20} holes/cm^3) and 0.85 (9.2×10^{19} electrons/cm^3) at 780 K, respectively. Therefore, $CuBiS_2$ is predicted as both an n-type and p-type potential low-cost thermoelectric material.

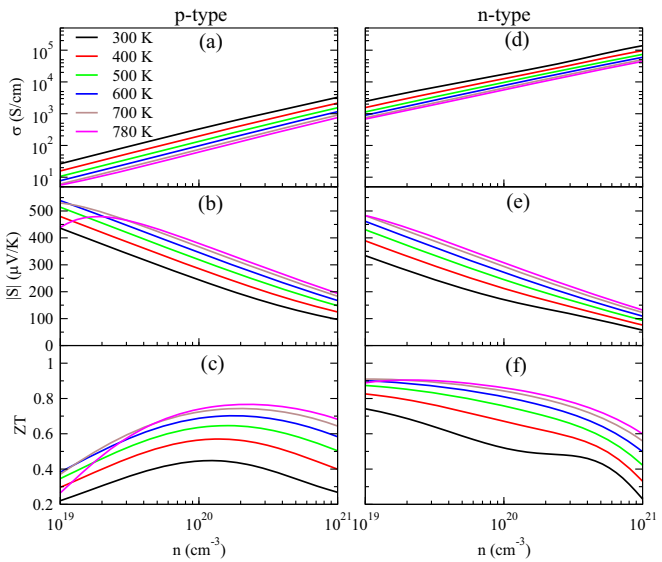

FIG. 8. The thermoelectric properties (σ, S, and ZT) of p-type (left) and n-type (right) $CuBiS_2$ at 300, 400, 500, 600, 700, and 780 K.

VI. CONCLUSION

Considering two isostructural natural compounds, $CuSbS_2$ and $CuBiS_2$, we found that lone-pair electrons would result in strong anharmonicity and hence reduce lattice thermal conductivity efficiently. The stereochemically active lone-pair electrons at the Sb sites are major contributors to the large Grüneisen parameters in $CuSbS_2$. However, in $CuBiS_2$, in addition to the lone-pair electrons at the Bi sites, the Cu ion rattling further raises the Grüneisen parameters. The larger Grüneisen parameters in $CuBiS_2$ lead to an ultralow thermal conductivity compared with $CuSbS_2$. Moreover, the highest ZT value in $CuBiS_2$ could reach 0.91 for the n-type doping at 700 K and 0.77 for the p-type doping at 780 K, which implies that good thermoelectric n- and p-type $CuBiS_2$ can be achieved using the same pristine compound. The ultralow lattice thermal conductivity and high figure of merit of $CuBiS_2$ not only indicate the possibility of using sulfosalt systematics as efficient thermoelectric materials but also

offer new insights for discovering and designing high-ZT thermoelectric materials with lone-pair electrons combined with the rattler atoms.

ACKNOWLEDGMENTS

The work was supported by the National Natural Science Foundation of China, Grants No. 11474283, No. 11547011, and No. 51371076, and the Major/Innovative Program of Development Foundation of the Hefei Center for Physical Science and Technology, Grant No. 2014FXCX001. The calculations were performed in Tianhe2 at the Beijing Computational Science Research Center and at the Center for Computational Science of CASHIPS, the ScGrid of the Supercomputing Center, and the Computer Network Information Center of the Chinese Academy of Science.

[1] B. Sales, D. Mandrus, and R. K. Williams, Science **272**, 1325 (1996).
[2] Y. Pei, H. Wang, and G. Snyder, Adv. Mater. **24**, 6125 (2012).
[3] W. Liu, X. Tan, K. Yin, H. Liu, X. Tang, J. Shi, Q. Zhang, and C. Uher, Phys. Rev. Lett. **108**, 166601 (2012).
[4] J. P. Heremans, V. Jovovic, E. S. Toberer, A. Saramat, K. Kurosaki, A. Charoenphakdee, S. Yamanaka, and G. J. Snyder, Science **321**, 554 (2008).
[5] C. Yu, T.-J. Zhu, R.-Z. Shi, Y. Zhang, X.-B. Zhao, and J. He, Acta Mater. **57**, 2757 (2009).
[6] H. Mun, S.-M. Choi, K. H. Lee, and S. W. Kim, ChemSusChem **8**, 2312 (2015).
[7] B. Poudel, Q. Hao, Y. Ma, Y. Lan, A. Minnich, B. Yu, X. Yan, D. Wang, A. Muto, D. Vashaee *et al.*, Science **320**, 634 (2008).
[8] Y. L. Yan and Y. X. Wang, J. Mater. Chem. **21**, 12497 (2011).
[9] S. R. Brown, S. M. Kauzlarich, F. Gascoin, and G. J. Snyder, Chem. Mater. **18**, 1873 (2006).
[10] L.-D. Zhao, S.-H. Lo, Y. Zhang, H. Sun, G. Tan, C. Uher, C. Wolverton, V. P. Dravid, and M. G. Kanatzidis, Nature (London) **508**, 373 (2014).
[11] M. Beekman and G. Nolas, J. Mater. Chem. **18**, 842 (2008).
[12] X. Shi, J. Yang, J. R. Salvador, M. Chi, J. Y. Cho, H. Wang, S. Bai, J. Yang, W. Zhang, and L. Chen, J. Am. Chem. Soc. **133**, 7837 (2011).
[13] S. N. Guin, A. Chatterjee, D. S. Negi, R. Datta, and K. Biswas, Energy Environ. Sci. **6**, 2603 (2013).
[14] S. N. Guin and K. Biswas, Chem. Mater. **25**, 3225 (2013).
[15] C. Xiao, X. Qin, J. Zhang, R. An, J. Xu, K. Li, B. Cao, J. Yang, B. Ye, and Y. Xie, J. Am. Chem. Soc. **134**, 18460 (2012).
[16] Y. Zhang, E. Skoug, J. Cain, V. Ozoliņš, D. Morelli, and C. Wolverton, Phys. Rev. B **85**, 054306 (2012).
[17] W. Lai, Y. Wang, D. T. Morelli, and X. Lu, Adv. Funct. Mater. **25**, 3648 (2015).
[18] W. Qiu, L. Wu, X. Ke, J. Yang, and W. Zhang, Sci. Rep. **5**, 13643 (2015).
[19] J. Zhou, G.-Q. Bian, Q.-Y. Zhu, Y. Zhang, C.-Y. Li, and J. Dai, J. Solid State Chem. **182**, 259 (2009).
[20] D. Spitzer, J. Phys. Chem. Solids **31**, 19 (1970).
[21] J. C. Portheine and W. Nowacki, Z. Kristallogr.-Cryst. Mater. **141**, 387 (1975).
[22] A. Kyono and M. Kimata, Am. Mineral. **90**, 162 (2005).
[23] P. E. Blöchl, Phys. Rev. B **50**, 17953 (1994).
[24] G. Kresse and J. Furthmüller, Comput. Mater. Sci. **6**, 15 (1996).
[25] H. J. Monkhorst and J. D. Pack, Phys. Rev. B **13**, 5188 (1976).
[26] E. Sjöstedt, L. Nordström, and D. Singh, Solid State Commun. **114**, 15 (2000).
[27] D. J. Singh and L. Nordstrom, *Planewaves, Pseudopotentials, and the LAPW Method*, 2nd ed. (Springer, New York, 2006).
[28] P. Blaha, K. Schwarz, G. Madsen, D. Kvasnicka, and J. Luitz, *WIEN2k: An Augmented Plane Wave + Local Orbitals Program for Calculating Crystal Properties* (Karlheinz Schwarz, Technical University at Wien, Austria, 2001).
[29] L. J. Sham and M. Schlüter, Phys. Rev. Lett. **51**, 1888 (1983).
[30] F. Tran and P. Blaha, Phys. Rev. Lett. **102**, 226401 (2009).
[31] G. K. Madsen and D. J. Singh, Comput. Phys. Commun. **175**, 67 (2006).
[32] A. Togo, F. Oba, and I. Tanaka, Phys. Rev. B **78**, 134106 (2008).
[33] D. T. Morelli, J. P. Heremans, and G. A. Slack, Phys. Rev. B **66**, 195304 (2002).
[34] M. Asen-Palmer, K. Bartkowski, E. Gmelin, M. Cardona, A. P. Zhernov, A. V. Inyushkin, A. Taldenkov, V. I. Ozhogin, K. M. Itoh, and E. E. Haller, Phys. Rev. B **56**, 9431 (1997).
[35] J. Callaway, Phys. Rev. **113**, 1046 (1959).
[36] G. A. Slack and S. Galginaitis, Phys. Rev. **133**, A253 (1964).
[37] G. Pizzi, D. Volja, B. Kozinsky, M. Fornari, and N. Marzari, Comput. Phys. Commun. **185**, 422 (2014).
[38] B. Himmetoglu, A. Janotti, H. Peelaers, A. Alkauskas, and C. G. Van de Walle, Phys. Rev. B **90**, 241204 (2014).
[39] A. F. May, E. S. Toberer, A. Saramat, and G. J. Snyder, Phys. Rev. B **80**, 125205 (2009).
[40] S.-H. Wei and A. Zunger, Phys. Rev. B **60**, 5404 (1999).
[41] A. Savin, O. Jepsen, J. Flad, O. K. Andersen, H. Preuss, and H. G. von Schnering, Angew. Chem., Int. Ed. Engl. **31**, 187 (1992).
[42] A. R. Gillespie and R. Nyholm, Q. Rev. Chem. Soc. **11**, 339 (1957).
[43] W. D. Callister and D. G. Rethwisch, *Materials Science and Engineering* (John Wiley & Sons, 2011).
[44] W. Qiu, L. Xi, P. Wei, X. Ke, J. Yang, and W. Zhang, Proc. Natl. Acad. Sci. USA **111**, 15031 (2014).
[45] D. Yang, W. Yao, Y. Yan, W. Qiu, L. Guo, X. Lu, C. Uher, X. Han, G. Wang, T. Yang, and Z. Xiaoyuan, NPG Asia Materials **9**, e387 (2017).
[46] Y. Xiao, C. Chang, Y. Pei, D. Wu, K. Peng, X. Zhou, S. Gong, J. He, Y. Zhang, Z. Zeng *et al.*, Phys. Rev. B **94**, 125203 (2016).
[47] E. J. Skoug and D. T. Morelli, Phys. Rev. Lett. **107**, 235901 (2011).
[48] See Supplemental Material at http://link.aps.org/supplemental/10.1103/PhysRevB.96.235205 for the band structures, effective masses, and electrical transport properties of the $CuSbS_2$ compound.
[49] M. Nair, C. Lopez-Mata, O. Gomez Daza, and P. Nair, Semicond. Sci. Technol. **18**, 755 (2003).
[50] R. Agaeva and O. Aliev, Inorg. Mater. **41**, 920 (2005).
[51] J. Heo, G. Laurita, S. Muir, M. A. Subramanian, and D. A. Keszler, Chem. Mater. **26**, 2047 (2014).